



Double Dots: Compact Pairs Mark Little Red Dots and High-Redshift Broad-line AGNs

A. J. BARGER ^{1,2,3} AND L. L. COWIE ³

¹*Department of Astronomy, University of Wisconsin-Madison, 475 N. Charter Street, Madison, WI 53706, USA*

²*Department of Physics and Astronomy, University of Hawaii, 2505 Correa Road, Honolulu, HI 96822, USA*

³*Institute for Astronomy, University of Hawaii, 2680 Woodlawn Drive, Honolulu, HI 96822, USA*

ABSTRACT

We utilize JWST imaging of the massive lensing cluster field A2744 to find close pairs of compact sources with separations less than $0''.25$. A large fraction of these “Double Dots” correspond to Little Red Dots (LRDs) or high-redshift broad-line active galactic nuclei (BLAGNs). Our analysis of 31 identified pairs reveals a median separation of $0''.15$. Statistical comparison against a uniform background shows that these are mostly physical pairs. We find that at least 16 of the 24 previously published LRDs in this field ($\sim 67\%$) are such pairs, as are both of the high-redshift BLAGNs. We demonstrate that the presence of a companion can significantly contaminate the measured spectral energy distribution, potentially masking the characteristic “v-shape” used for LRD classification. Furthermore, our 2D spectroscopic analysis of several pairs reveals that BLAGN activity is not confined to the redder member of the pair but can originate in either one. Since most LRDs contain broad emission lines, our findings suggest that close pairs are extremely effective markers of galaxies with broad lines at high redshift. We speculate on possible mechanisms, concluding that we are likely seeing merger-driven accretion.

1. INTRODUCTION

JWST observations have shown that broad-line sources are surprisingly common at high redshift ($z = 4 - 7$). This includes both blue broad-line active galactic nuclei (BLAGNs; Y. Harikane et al. 2023) and Little Red Dots (LRDs; J. Matthee et al. 2024; J. E. Greene et al. 2024; I. Labbe et al. 2025; D. D. Kocevski et al. 2025), most of whose spectra show broad-line $H\alpha$ (e.g., A. J. Taylor et al. 2025).

Currently, the favored interpretation of the LRDs is that they are high-redshift supermassive black holes, as supported by the detection of the broad Balmer emission lines. There are still many questions about this interpretation, however. Their black hole masses would be only 10^6 to $10^8 M_{\odot}$, which is orders of magnitude lower in mass than the luminous quasars accessible before JWST (Y. Harikane et al. 2023; R. Maiolino et al. 2024; J. Matthee et al. 2024).

In addition to their abundance, LRDs have very unusual properties: they are systematically overmassive relative to their host galaxies based on local scaling relations, and they are strikingly weak in X-ray, mid-infrared, submillimeter, and radio emission (T. T. Ananna et al. 2024; A. J. Barger et al. 2026; G. Mazzolari et al. 2026). The LRDs appear to represent the higher luminosity end of the BLAGN population (A. J.

Taylor et al. 2025), though whether they are physically distinct or simply the most obscured examples remains unclear.

Indeed, driven by these problems, alternatives to the BLAGN picture continue to be put forward. Most recently, J. Chisholm et al. (2026) have proposed that LRDs may instead be globular clusters in formation, with the rest-frame UV arising from a very young stellar population, and the rest-frame optical dominated by short-lived supermassive stars.

Accepting the BLAGN interpretation, we still need very unusual accretion properties to account for the observations and high-mass seeds to explain their overmassive nature. The lack of significant X-ray emission suggests they may be in a super-Eddington accretion regime where “slim” accretion disks with high-density coronae can lead to softer X-ray spectra and suppressed coronal emission (F. Pacucci & R. Narayan 2024). The characteristic “v-shape” spectral energy distribution (SED) has been interpreted as the signature of dense gas enshrouding the AGN (J. E. Greene et al. 2024; J. Matthee et al. 2024). The high masses may be explained by the Direct Collapse Black Hole (DCBH) model (A. Loeb & F. A. Rasio 1994; M. Volonteri & M. J. Rees 2005; M. C. Begelman et al. 2006; G. Lodato & P. Natarajan 2006, 2007), where the high-mass seeds can form when the Lyman-Werner cooling is suppressed by the radiation from a neighboring galaxy (F. Pacucci et al. 2026). This would require the presence of a companion object irradiating the collapsing cloud, a configuration that would

predict a high incidence of close pairs (J. F. W. Baggen et al. 2026).

Nearly all of the possibilities we have discussed above, including merger-driven accretion, direct black hole formation, and globular cluster formation would likely imply that the objects should have complex substructure. Treating them as single objects may just reflect the key limitation of spatial resolution. At the angular scales probed by the F444W band of JWST, what appears to be a single compact source may in fact be two or more physically associated objects blended together. If high redshift broad-line sources and LRDs frequently contain close pairs, the implications would be significant: their SEDs would be contaminated by companion light, their photometric classifications would be systematically biased, and the spectroscopic signatures used to identify broad-line activity might be attributed to the wrong component.

In this paper, we exploit the exceptional depth of JWST imaging and enhanced resolution in the lensing cluster field A2744 (T. Treu et al. 2022; R. Bezanson et al. 2024; J. R. Weaver et al. 2024) to search systematically for such close pairs among compact sources. We identify 31 compact pairs — which we term “Double Dots” — with a median (not delensed) separation of just 0.15 arcseconds. We find that at least 16 of the 24 previously published LRDs in this field (J. E. Greene et al. 2024; I. Labbe et al. 2025; D. D. Kocevski et al. 2026) correspond to such pairs, and we demonstrate through SED decomposition and 2D spectroscopic analysis that companion contamination has significant effects. Strikingly, and consistent with the broader JWST picture of high-redshift broad-line AGN (Y. Harikane et al. 2023), the AGN activity in these pairs is not confined to the redder component, suggesting that close pairs may serve as a fundamental marker of high-redshift AGN.

The paper is structured as follows. In Section 2, we describe our selection. In Section 3, we present our analysis of the SEDs and spectra in the pairs. Finally, in Section 4, we summarize our results and consider possible interpretation.

We assume a standard cosmology of $H_0 = 70.5 \text{ km s}^{-1} \text{ Mpc}^{-1}$, $\Omega_M = 0.27$, and $\Omega_\Lambda = 0.73$ (D. Larson et al. 2011). In calculating masses and SFRs, we assume a P. Kroupa (2001) initial mass function.

2. DATA

2.1. JWST imaging

The A2744 field has JWST observations from several surveys, including the GLASS-A2744 (T. Treu et al. 2022) and UNCOVER (R. Bezanson et al. 2024) programs. Here we use the DR2 photometric catalog from J. R. Weaver et al. (2024), which contains additional data products provided by the UNCOVER team, including lensing magnifications, photometric and spectroscopic redshifts, and rest-frame HST and JWST fluxes in many bands. The provided lensing magnifications

were derived from the lensing model of L. J. Furtak et al. (2023a), which is highly constrained using HST and JWST multiply-imaged sources.

We started by identifying moderately compact sources (FWHM $< 0''.2$ in F444W) with $S/N > 20$ in the F444W band, which were not identified as stars. The FWHMs are the observed values without any deconvolution of the point spread function or correction for lensing. After a first-pass visual inspection to confirm the sources were real, we compiled a list of 153 sources. This list contains all 24 published LRDs in the field (J. E. Greene et al. 2024; I. Labbe et al. 2025; D. D. Kocevski et al. 2025), excluding one brown dwarf and one source with S/N below 20 in the F444W band.

Next, we visually identified which of these sources are double in F150W, which we define here as having two or more sources in a $0''.25$ radius region (31 pairs; see Table 1 where we give the coordinates for all of the pairs). We refer to this as *our compact pairs sample* and label the individual objects DD0 to DD61. These sources are generally unresolved in F444W and appear as a single compact source at this wavelength (e.g. Figure 4). Eleven of the 24 published LRDs, as well as the two BLAGNs found in the field by Y. Harikane et al. (2023) are contained in this sample, as noted in the table. As noted in the Introduction, since most of the LRDs contain broad lines, it appears that the close pairs are extremely effective markers of high-redshift broad line sources in the field.

We measured the source size of each member of a pair using two 2D Gaussians fit to the F150 image using the IDL MPFIT routine (C. B. Markwardt 2009). We illustrate the procedure in Figure 1. For each member of the pair, we fit a 2D Gaussian with separate measures of the x and y widths. We take the FWHM to be the geometric mean of the FWHM measured in each of the two axes. This leaves us with measurements of the sizes of the two members of the pair (see Table 1). (The FWHM of the PSF at this wavelength is $0''.05$, though it is slightly undersampled in the NIRCAM image).

The double fitting also provides an accurate measure of the pair separation. The median separation is $0''.15$, though one of the sources has an offset slightly larger than $0''.25$. The distribution is skewed to smaller separations (Figure 2), suggesting that these are physical pairs rather than chance projections. A Chi-Square analysis comparing with the values expected from a uniform background model gives a p-value of only 5.2×10^{-7} strongly rejecting the hypothesis that the sources are drawn from the background population.

The steep rise to smaller separations suggests that there may be LRDs with closer separations than would be included in our pairs sample. We therefore searched the full LRD sample in a combined F115W and F150W image to see if cases with more closely separated pairs might be found. A further 5 objects have companions with closer separations. We show one example in Fig-

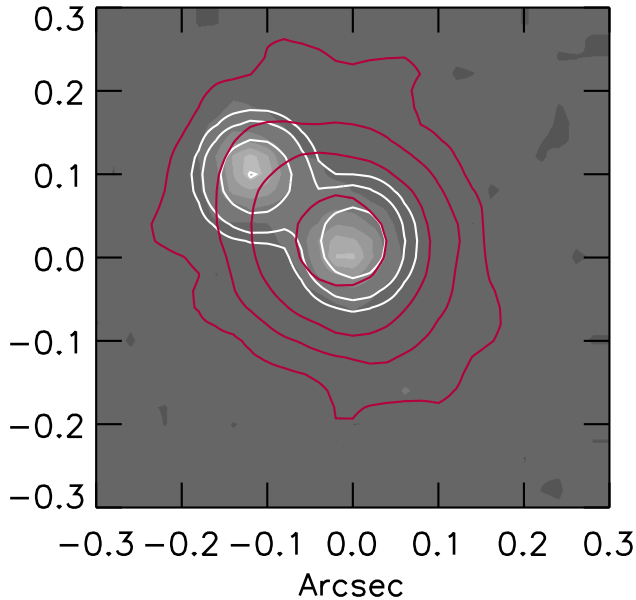


Figure 1. Illustration of the fitting procedure. We show the F150W image of the pair DD20 and DD21. Overlaid (white contours) are the two 2D Gaussian fits to the F150W image. Each has a fitted x and y width; in this case, the fits are near circular. We use the geometric mean of the x and y measurements for each member of the pair as the FWHM of that component. Here, both components have FWHM = $0''.083$ (see Table 1). Also overlaid is the F444W image (red contours), illustrating how strongly concentrated the F444W light is on the lower right member of the pair.

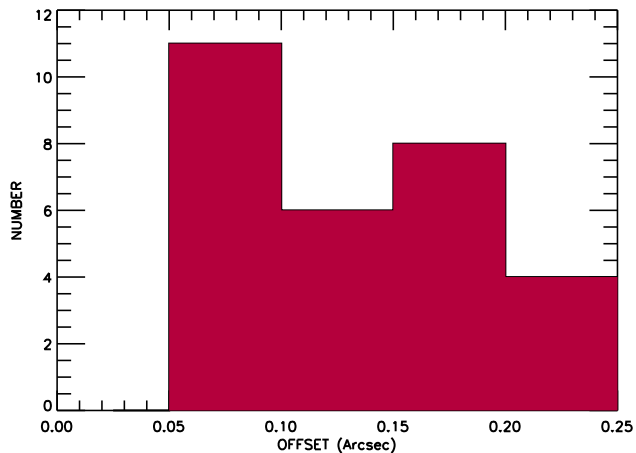


Figure 2. The distribution of offsets between the pairs. We cannot measure offsets smaller than $0''.05$ given the spatial resolution in the F150 image. However, at larger separations, the distribution is skewed to smaller values, which is not consistent with expectations for a background population.

ure 3. In total, at least 16 of the 24 previously published LRDs in this field are pairs.

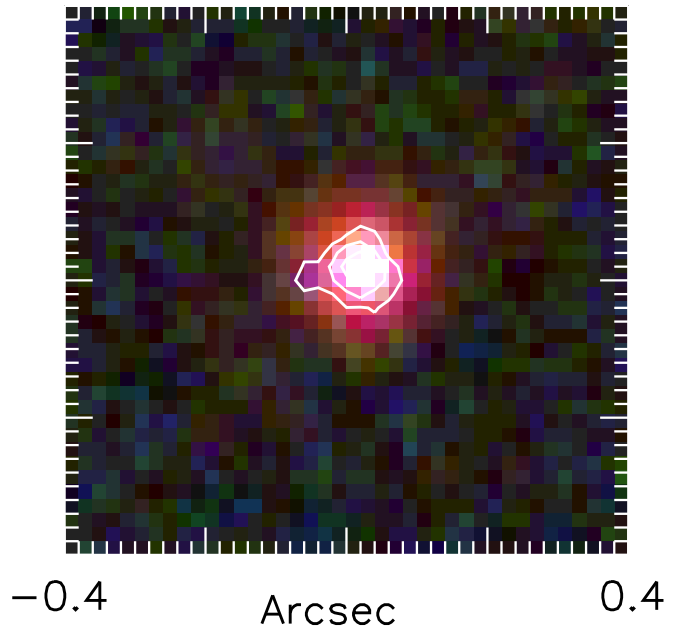


Figure 3. RGB images (F444W, F200W, and F150W) for an LRD (R.A. 3.5694625, Decl. -30.339306) from I. Labbe et al. (2025). Overlaid (white contours) is the combined F115W and F150W image. The companion is $0''.05$ separated from the peak and is just below the limit where it would be included in our pairs sample.

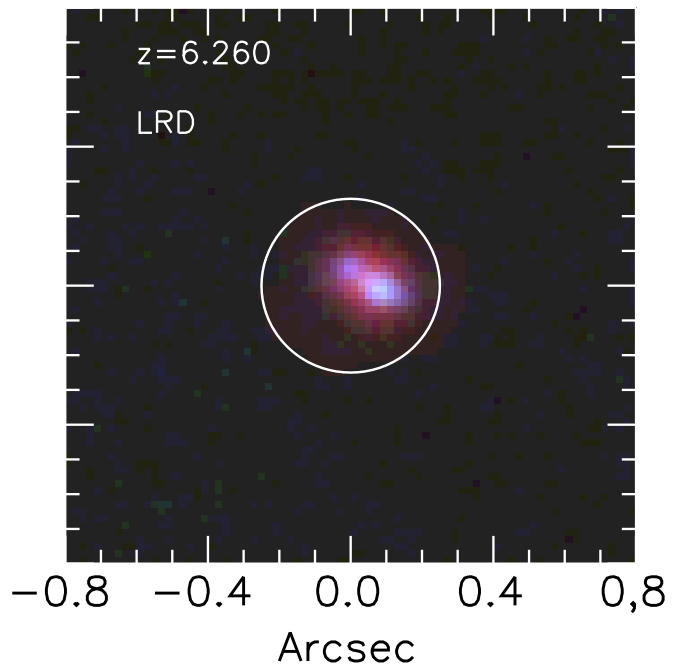


Figure 4. RGB images (F444W, F200W, and F150W) for the one pair in our sample (DD54 and DD55) that consists of two red sources. White circle shows a $0''.25$ radius.

Up to this point, we have considered only the sizes and separations of the sources. However, it is clear that

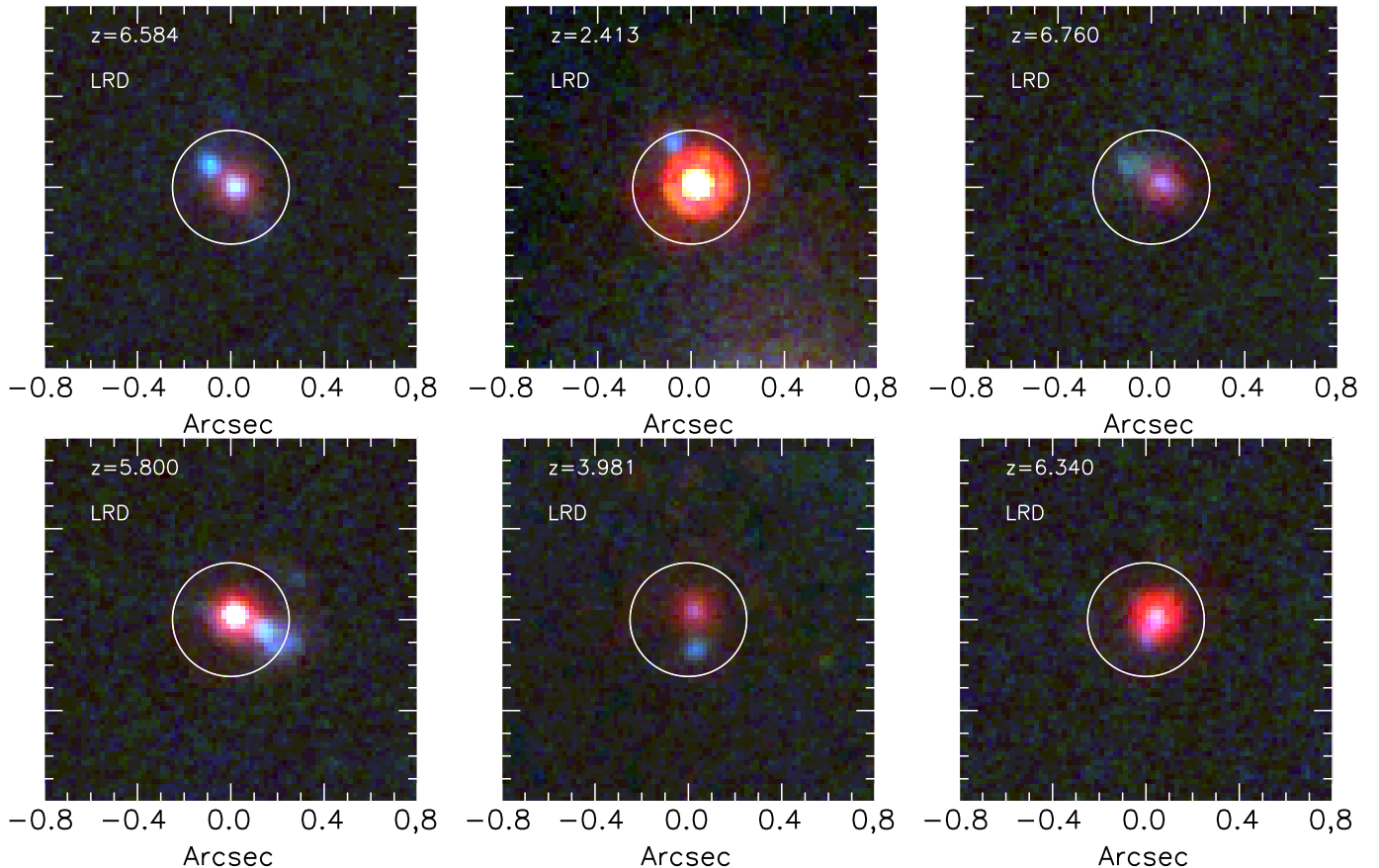


Figure 5. RGB images (F444W, F200W, and F150W) for six of the LRDs (DD20, DD14, DD58, DD34, DD16, and DD22) with a neighboring blue companion. The white circle shows a $0''.25$ radius. In all cases, the blue companion is within $0''.25$ of the LRD. We show the redshift in the upper left corner. All of these sources have spectroscopic redshifts and have been classified as LRDs in the literature. [M. Golubchik et al. \(2025\)](#) found a similar pair behind the cluster A383.

adding the pairs criterion significantly increases the fractional LRD selection. Thus, we have 11 published LRDs out of 31 sources in the compact pairs sample versus 24 out of 153 in the full compact sample.

More specifically, there are a large fraction of the pairs with one blue and one red member. Only one pair has two red members, while a number of pairs have two blue members. For each member of a pair, we measured the fluxes over the full available bands. We measured the counts in each component using the Gaussian fit and converted this to the flux. In Table 2, we give the fluxes of the pairs in μJy . Unlike the UNCOVER fluxes aperture correction so, in comparing the combined fluxes with the uncover data, we need to correct for this offset. (See Figure 8). We then used the SED for each individual member to determine if it is an LRD.

Different papers have adopted different selection criteria for determining whether a source is an LRD. We use the power-law fitting method of [D. D. Kocevski et al. \(2025\)](#), which compares power law fits to the shapes of the rest-frame UV and optical portions of the SED to determine whether the source has the v-shape that is characteristic of an LRD. V-shaped sources have power

law indices β ($f_\lambda \propto \lambda^\beta$) less than -0.37 in the rest frame UV and larger than 0 in the rest frame optical. We note that separating the pairs can make it easier for one member to satisfy this criterion. We find that 14 of the pairs have at least one member that does (labeled “v-shape” in the last column of Table 1), 11 of which are already included in the known LRD sample.

The pair DD54 and DD55 is unique in containing two red members, one of which individually satisfies the v-shape criterion. In Figure 4, we show the image of this pair. The more common pairing is an LRD with a blue companion (see Figure 5), or a pair of blue sources.

2.2. Spectra

We next searched the JWST DAWN archive ([K. E. Heintz et al. 2025](#)) for sources with NIRSpec slit spectra whose orientation is such that the spectra overlay both members of the pair and where the separation is large enough that we can distinguish the two sources. We used the overlay program in the DAWN archive ([R. Hausen & B. E. Robertson 2022](#)) to find the spectra that were suitable for this purpose. We found useful spectra for the pairs DD16 and DD17; DD34 and DD35; DD54

and DD55; and DD58 and DD59. We then downloaded the reduced NIRSpec spectra for these sources from the DAWN archive (A. de Graaff et al. 2025). We did not attempt to use WFSS spectra.

The spectra for the pair DD16 and DD17 are the clearest, both because of their wider separation ($0''.165$) and because of the high resolution and high S/N G130M spectra from PID 09214 (PI C. Mason). In Figure 6 (left panel), we show the NIRSpec slit (white lines) overlaid on the pair, illustrating that both members are well covered by the slit. We also show contour plots of the [OIII]5007 (blue) and H α (red) lines in the spectra. The x position and scale is arbitrary, but the y -axis is matched to the image, and the position of the peaks in the spectra correspond to the object positions (horizontal gold lines). The red source in the pair has stronger H α emission, while the blue source has stronger [OIII]5007 emission. The two components show a velocity separation of 145 km s^{-1} (see Figure 7). We discuss the spectra further below.

In Figure 6 (right panel), we show a similar plot for the pair DD34 and DD35 from PID 02561 (PI Labbe). Here, both sources lie within the slit, but they are closer ($0''.149$) and more diffuse, resulting in more blending in the spectral image. This PRISM spectrum has lower resolution ($R \sim 350$), which makes the relative velocity structure in the two sources harder to differentiate visually. However, the [OIII]5007 emission line is clearly more weighted to the blue source than the H α emission line, which is strongest in the red source.

There are two spectra for the pair DD54 and DD55: a PRISM spectrum from PID 02561 (PI Labbe) and a G395M spectrum from PID 06053 (PI Wold). The Wold spectrum is of much higher quality, but it is slightly misaligned with the slit, resulting in the lines from the two sources being blended. The Labbe spectrum shows the H α emission line with a peak at the position of the reddest source and the [OIII]5007 emission line displaced towards the second member of the pair. The pair DD58 and DD59 has only a PRISM spectrum from Labbe. In this case, it is unclear whether the blue member of the pair is present in the emission lines.

3. DISCUSSION

3.1. SEDs

The most direct effect of the doubles is that we may fail to determine properly the SEDs of the sources, and, in particular, to identify an LRD due to contamination by its neighbor. The composite SEDs contain contributions from both members of the pair, and the blue members may contribute a substantial part of the rest-frame UV flux; in some cases, they may dominate at these wavelengths (see Table 2). Pairs of this type include DD20,DD21, DD30,DD31, DD32,DD33, and DD58,DD59.

In Figure 8, we show an example of this effect for the DD30 and DD31 pair. Here, the composite SED (purple

squares) marginally fails to meet the v-shape criterion for LRD selection, having too flat a rest-frame optical SED. However, DD30 (red squares) does meet the v-shape criterion. DD31 (blue squares) appears to be a relatively unobscured star-forming galaxy based on its flat SED.

For all 11 pairs in the sample whose composite SEDs were previously classified as LRDs, we find one member's SED individually meets the v-shape criterion. However, in a further three pairs, including the DD30 and DD31 pair shown in Figure 8, we find that one member's SED also individually meets the v-shape criterion, but that fact was previously hidden due to the contribution from the companion.

3.2. 2D Spectra

An interesting question to ask is, from which member of the pair do broad lines arise? For example, the Y. Harikane et al. (2023) sources, which correspond to the DD2 and DD3 and DD4 and DD5 pairs, are BLAGNs, so we may investigate which member hosts the AGN when the broad line is seen in the 2D spectra.

For the DD4 and DD5 pair, we have two spectra. The Treu spectrum (PID 01324), which was used by Y. Harikane et al. (2023), is centered on the blue member and clearly shows the broad line in H α . A later spectrum from Mason (Program ID 09214) is centered on the red member and does not clearly show the broad line in H α . We conclude that, in this case, it is the blue member that hosts the AGN.

In Figure 9, we show the DD58 and DD59 pair. Here, the broad line can be clearly seen in H α (center panel), and, more marginally, in H β (right panel). For both emission lines, the broad line appears to arise in the northerly member of the pair (DD59; see slit configuration in left panel). The LRD (DD58) seems to contain only narrow lines.

In Figure 10, we show the DD34 and DD35 pair. Here, the broad line appears to coincide instead with the LRD (i.e., DD34; upper red source). The blue companion (DD35) has narrow emission lines.

In conclusion, the broad line can arise in either component of the pair. It does not necessarily arise in an LRD member or in the redder member of a pair.

4. INTERPRETATION

We have demonstrated that substructure seems to be a common feature of the broad-line systems at high redshift, and, in particular, of the LRDs. In Figure 11, we show the demagnified physical separations of the pairs vs. redshift. We highlight with red circles pairs where at least one member has broad lines or a v-shape. Separations range from 0.3 to 1.7 kpc and show little dependence on redshift. The range of separations appears similar for both populations, for which there are a number of possible explanations.

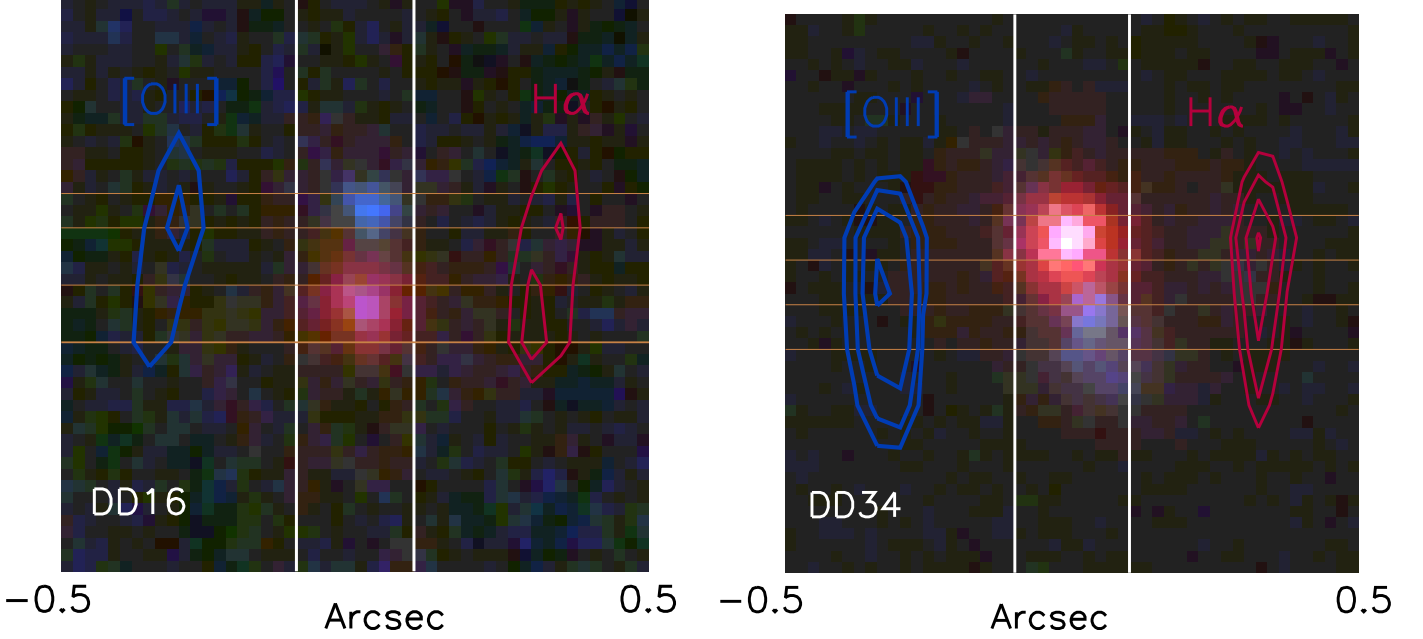


Figure 6. RGB images (F444W, F200W, and F150W) for two of the pairs where the slit for the NIRSpc spectrum was roughly aligned to cover both sources in the pair (slit position marked by vertical white lines): (left panel) DD16 and DD17 and (right panel) DD34 and DD35. Both of these pairs have fairly wide separations ($0''.165$ and $0''.149$, respectively), making it possible to see the spatial structure in the emission lines. In each panel, we show a contour plot of the (left) [OIII]5007 (blue) and (right) H α (red) emission lines. The horizontal gold lines mark the positions of the two members of the pairs. For both pairs, the emission lines extend over both sources, and we can see a small velocity offset between the two.

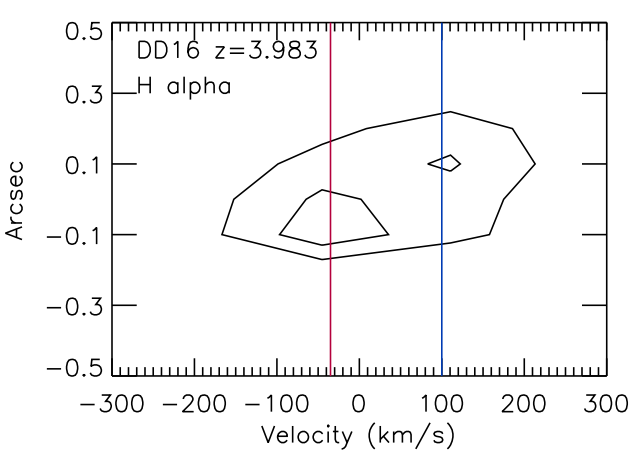


Figure 7. Contour plot of the 2D spectral image of the H α emission line in the DD16 and DD17 pair. The red and blue vertical lines show, respectively, the velocities of the red (DD16) and blue (DD17) sources, with a velocity separation of 145 km s^{-1} .

The most straightforward interpretation may be that the substructure represents galaxy mergers triggering AGN activity and shrouding the system in gas and dust. This would naturally explain why close pairs are such strong markers of BLAGNs and could also explain many of the unusual properties of LRDs.

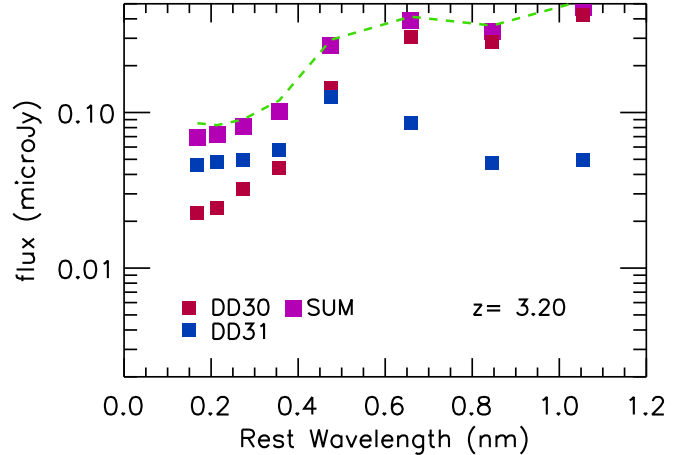


Figure 8. Relative SEDs of the DD30 (red squares) and DD31 (blue squares) pair. The combined fluxes are shown in purple and closely match the UNCOVER catalog fluxes when the aperture correction used for the UNCOVER fluxes is removed (green dashed curve). DD31 dominates the fluxes in the rest-frame UV, and DD30 in the rest-frame optical.

However, there might also have been enhancement of supermassive black hole growth if a DCBH formed due to the presence of a companion, which allowed early collapse of a seed black hole by suppressing molecular H cooling (J. F. W. Baggen et al. 2026). This could have driven the growth of the black hole in one of the pair.

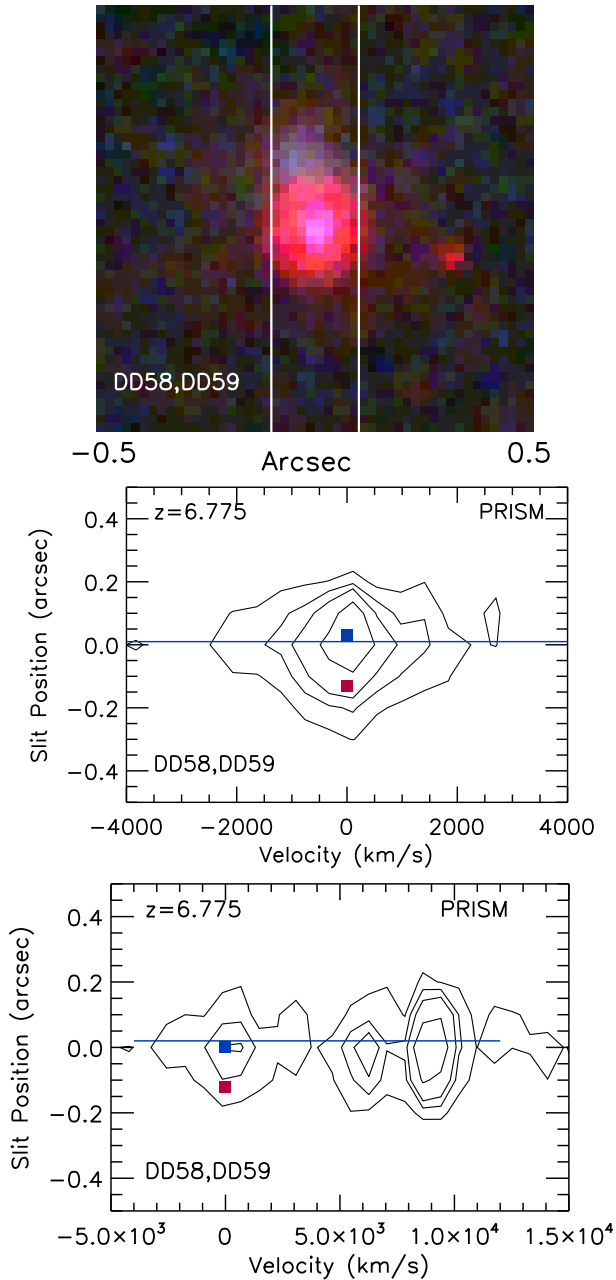


Figure 9. 2D spectra of the pair DD58 and DD59. (Top) Orientation along the slit. DD58 is the lower, redder object, and DD59 is the upper, bluer object. (Middle) 2D spectrum of $H\alpha$. (Bottom) 2D spectrum of the $H\beta$ and [OIII] region. The broad line is easily visible and marked in each panel with the horizontal blue line. The relative source positions are shown with the blue (DD59) and red (DD58) squares. The broad lines are clearly associated with the blue companion DD59 and not with the LRD DD58.

Then, as the pair begins to merge, it could trigger a super-Eddington accretion event shrouded in dust.

However, we should also bear in mind the possibility that these are not AGNs at all and that the substructure

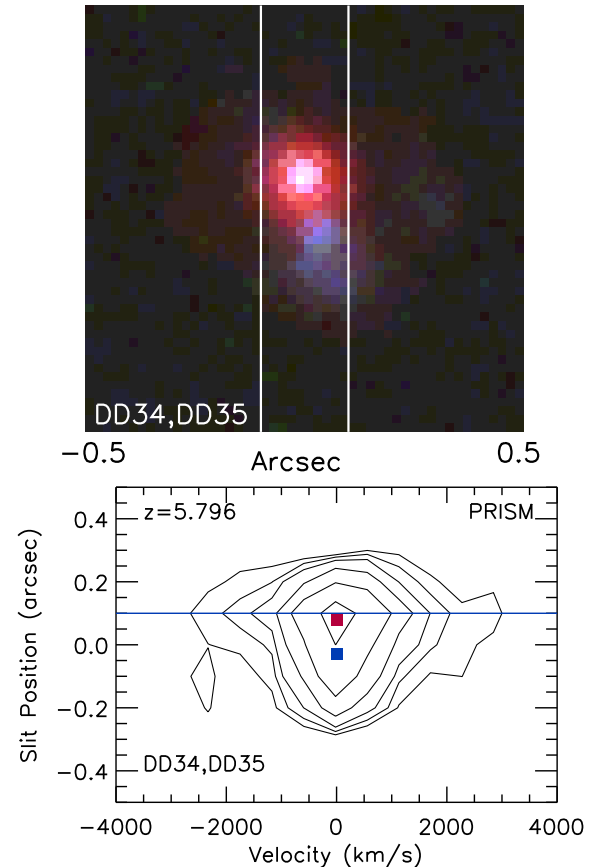


Figure 10. 2D spectra of the pair DD34 and DD35. (Top) Orientation along the slit. DD34 is the upper, redder object, and DD35 is the lower, bluer object. (Bottom) 2D spectrum of $H\alpha$. The broad line is easily visible and marked with the horizontal blue line. The relative source positions are shown with the blue (DD35) and red (DD34) squares. The broad line is clearly associated with the LRD DD34.

reflects the formation of globular clusters, as in the [J. Chisholm et al. \(2026\)](#) model.

Here we focus on the accretion model. We first computed the stellar masses of each of the members using the rest-frame demagnified J -band luminosity. For the higher redshift sources, this involves a substantial extrapolation. The highest value is a logarithmic mass of $9.5 M_{\odot}$, and the median value is $6.9 M_{\odot}$. Given the possible contributions of the AGNs, these may be best viewed as upper limits. Given these uncertainties, a more sophisticated SED fitting calculation does not seem justified.

We can determine whether the pairs might be merging based on their masses, physical separations, and velocity separations. We demagnified all quantities using the mean pair lensing magnification from the UNCOVER lensing model ([L. J. Furtak et al. 2023b](#)). In Table 3, we summarize the magnifications (μ), the adopted redshifts (z_{spec} , where available, and otherwise z_{phot} , as given in

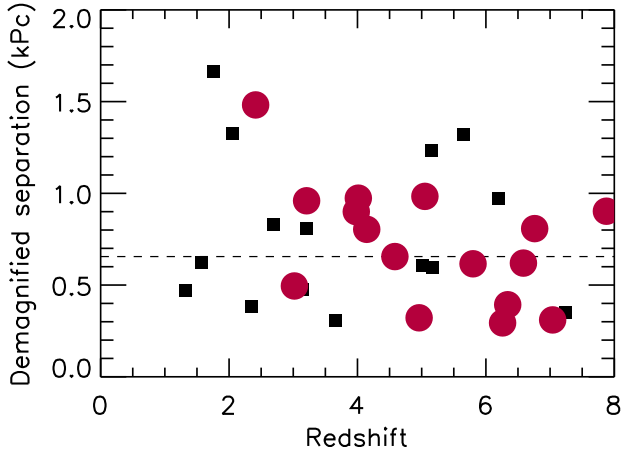


Figure 11. Physical separation of the pairs vs. redshift. The separations are corrected for lensing (see text). The red circles highlight pairs where at least one member has broad lines or a v shape. The horizontal dashed line shows the median separation of the sample.

Table 1), and observed separations (θ), together with the delensed physical separations (r) and the delensed stellar masses of the two members ($r = r_{\text{obs}}/\sqrt{\mu}$ and $M_{\star} = M_{\star}^{\text{obs}}/\mu$; the latter are labeled as either “A” or “B” in the order of the listed IDs of the members).

We calculate total masses (M_{tot}) assuming a dark matter ratio of 30, and we combine these masses with the physical separations to compute escape velocities (v_{esc}).

We also provide the mass ratio (q) and the merger type based on the mass ratio: major ($q > 0.25$), minor ($0.10 < q \leq 0.25$), and satellite ($q \leq 0.10$).

In Figure 12, we show the escape velocity of the pairs versus redshift. We highlight with red circles sources where at least one member has broad lines or a v shape. The results appear strongly consistent with the accretion hypothesis. The red circles sources are much more tightly bound. Of the 21 pairs with escape velocities $> 200 \text{ km s}^{-1}$, 17 have LRD or BLAGN signatures. Meanwhile, only one (DD16 and DD17) of the 10 more weakly bound pairs does. In this case, the small velocity separation in the spectra would also be consistent with the pair being bound.

5. SUMMARY

We used deep JWST imaging of the lensing cluster field A2744 to search systematically for close pairs among compact sources. We identified 31 “Double Dot” pairs with separations $< 0''.25$ and a median separation of $0''.15$. We compared these with sources in the field that were previously classified as LRDs or BLAGNs. Our main findings are as follows:

1. At least 16 of the 24 previously published LRDs in the A2744 field ($\sim 67\%$) are members of close pairs, as are both of the high-redshift BLAGNs identified by Y. Harikane et al. (2023). Since most

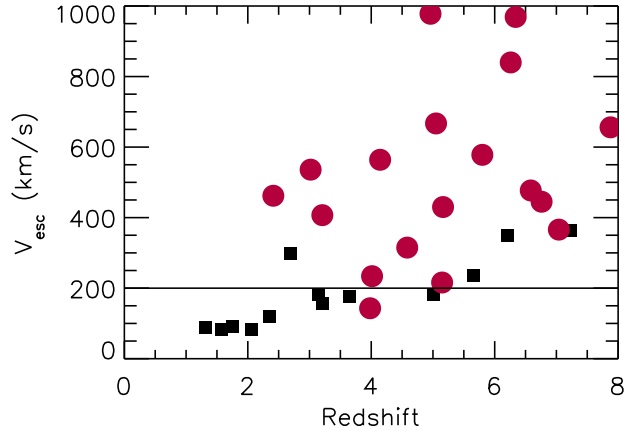


Figure 12. Escape velocity of the pairs vs. redshift. The red circles highlight pairs where at least one member has broad lines or a v shape. The horizontal line shows a velocity of 200 km s^{-1} . 17 of the 21 sources lying above this are either BLAGNs (BLAGNs are labeled as such in the Class column of Table 3) or have v shapes (v shapes are marked by daggers in the ID column of Table 3). Only one of the 10 more weakly bound pairs does.

LRDs contain broad emission lines, close pairs are therefore extremely effective markers of galaxies with broad lines at high redshift.

2. We found that companion contamination can significantly distort SED measurements. The blue companion in a pair may dominate the rest-frame UV flux, which can mask the “v-shape” signature used to classify LRDs. When we decomposed the pairs and analyzed each member individually, we found three additional sources that satisfied the v-shape criterion for an LRD.
3. We performed 2D spectroscopic analysis of four pairs, finding that broad emission lines can arise in either member of the pair; they are not confined to the redder or LRD component. For example, in the pair DD58 and DD59, broad lines originate in the blue companion DD59, while in the pair DD34 and DD35, in the LRD DD34.
4. We determined that sources with escape velocities $> 200 \text{ km s}^{-1}$ overwhelmingly showed broad lines or a v shape (17 of 21), while in the more weakly bound pairs, only 1 of 10 did. This is strongly consistent with a merger-driven accretion scenario.

Table 1. Compact Pairs Sample

ID	Offset (arcsec)	R.A. (deg)	Decl. (deg)	FWHM (arcsec)	z_{phot}	z_{spec}	Class	v shape
(1)	(2)	(3)	(4)	(5)	(6)	(7)	(8)	(9)
0	0.118	3.6326168	-30.436611	0.079	2.686
1	...	3.6325788	-30.436666	0.188
2	0.178	3.5803041	-30.424389	0.073	...	4.013	BLAGN	...
3	...	3.5802500	-30.424389	0.169
4	0.127	3.5771418	-30.422527	0.083	...	4.583	BLAGN	...
5	...	3.5771585	-30.422556	0.115
6	0.133	3.6081877	-30.422001	0.070	...	5.015
7	...	3.6082001	-30.421972	0.073
8	0.081	3.5537708	-30.410110	0.075	7.235
9	...	3.5537875	-30.410110	0.068
10	0.077	3.5789330	-30.408138	0.065	2.347
11	...	3.5789042	-30.408138	0.103
12	0.068	3.5775459	-30.407444	0.072	3.650
13	...	3.5775540	-30.407473	0.150
14	0.211	3.5567081	-30.408167	0.068	...	2.414	LRD	yes
15	...	3.5567374	-30.408138	0.069
16	0.165	3.5677586	-30.407278	0.076	...	3.982	LRD	yes
17	...	3.5677626	-30.407251	0.075
18	0.184	3.5508418	-30.406584	0.070	...	5.050	LRD	yes
19	...	3.5507791	-30.406610	0.184
20	0.152	3.6125040	-30.400583	0.083	...	6.585	LRD	yes
21	...	3.6125374	-30.400555	0.083
22	0.087	3.6206081	-30.399944	0.076	...	6.340	LRD	yes
23	...	3.6206207	-30.399971	0.095
24	0.186	3.5330207	-30.386862	0.112	2.060
25	...	3.5329959	-30.386889	0.177
26	0.263	3.6236458	-30.384249	0.091	...	5.651
27	...	3.6236210	-30.384306	0.077
28	0.251	3.6138084	-30.382999	0.082	5.148
29	...	3.6138418	-30.382917	0.115
30	0.181	3.5967584	-30.382557	0.082	3.208	yes
31	...	3.5967040	-30.382557	0.125
32	0.065	3.6179543	-30.381834	0.069	1.318
33	...	3.6179709	-30.381805	0.125

Table 1 *continued*

Table 1 (*continued*)

ID	Offset (arcsec)	R.A. (deg)	Decl. (deg)	FWHM (arcsec)	z_{phot}	z_{spec}	Class	v shape
(1)	(2)	(3)	(4)	(5)	(6)	(7)	(8)	(9)
34	0.149	3.5428374	-30.380638	0.065	...	5.800	LRD	yes
35	...	3.5427957	-30.380638	0.161
36	0.242	3.6045001	-30.380445	0.096	...	7.877	...	yes
37	...	3.6045625	-30.380388	0.137
38	0.226	3.5328708	-30.379862	0.097	...	6.203
39	...	3.5328500	-30.379917	0.070
40	0.122	3.6291165	-30.378445	0.070	3.209
41	...	3.6291039	-30.378416	0.146
42	0.228	3.5143626	-30.377140	0.149	1.759
43	...	3.5142877	-30.377167	0.139
44	0.100	3.5337749	-30.376446	0.069	1.566
45	...	3.5337584	-30.376446	0.139
46	0.149	3.5838125	-30.374500	0.112	5.164
47	...	3.5838542	-30.374527	0.091
48	0.080	3.5194333	-30.375139	0.071	3.018	yes
49	...	3.5194249	-30.375168	0.080
50	0.110	3.5696080	-30.373247	0.086	...	7.040	LRD	yes
51	...	3.5695920	-30.373220	0.127
52	0.082	3.5190916	-30.371307	0.103	3.142
53	...	3.5190876	-30.371279	0.092
54	0.091	3.5790000	-30.362583	0.108	...	6.260	LRD	yes
55	...	3.5789750	-30.362583	0.093
56	0.057	3.5299833	-30.358112	0.071	...	4.963	LRD	yes
57	...	3.5299666	-30.358112	0.108
58	0.172	3.5339832	-30.353306	0.140	...	6.760	LRD	yes
59	...	3.5340335	-30.353277	0.115
60	0.158	3.6102083	-30.421000	0.082	4.144	...	LRD	yes
61	...	3.6101875	-30.421028	0.137

NOTE— (1) ID, (2) offset between the two members of each pair rounded to three decimal places, (3) Right Ascension, (4) Declination, (5) FWHM rounded to three decimal places, (6) photometric redshift, (7) spectroscopic redshift, (8) previously identified class (BLAGN or LRD), and (9) whether the member of the pair satisfies the v-shape criterion for an LRD from [D. D. Kocevski et al. \(2025\)](#). To maintain clarity for the pairs, we only list redshift values for the primary member of each pair (i.e., even IDs).

Table 2. Photometry for the Compact Pairs Sample

ID	z	F70W (μJy)	F90W (μJy)	F115W (μJy)	F150W (μJy)	F200W (μJy)	F277W (μJy)	F356W (μJy)	F444W (μJy)
(1)	(2)	(3)	(4)	(5)	(6)	(7)	(8)	(9)	(10)
0	2.686	0.000	0.000	0.069	0.088	0.177	0.109	0.098	0.154
1	2.686	0.000	0.000	0.046	0.048	0.082	0.033	0.035	0.037
2	4.013	0.024	0.036	0.041	0.054	0.076	0.196	0.140	0.077
3	4.013	0.022	0.024	0.018	0.021	0.026	0.042	0.028	0.013
4	4.583	0.019	0.033	0.037	0.036	0.048	0.118	0.100	0.083
5	4.583	0.012	0.020	0.022	0.022	0.023	0.026	0.021	0.006
6	5.015	0.011	0.015	0.014	0.013	0.017	0.034	0.020	0.025
7	5.015	0.007	0.004	0.003	0.006	0.002	0.000	0.001	0.003
8	7.235	-0.001	0.000	0.009	0.010	0.007	0.011	0.011	0.020
9	7.235	0.001	0.001	0.006	0.006	0.008	0.004	0.003	0.008
10	2.347	0.031	0.029	0.029	0.032	0.032	0.032	0.031	0.030
11	2.347	0.023	0.021	0.016	0.029	0.020	0.010	0.009	0.008
12	3.650	0.027	0.027	0.023	0.022	0.028	0.037	0.016	0.019
13	3.650	0.015	0.014	0.016	0.020	0.014	0.020	0.009	0.010
14	2.414	0.016	0.018	0.023	0.046	0.152	0.504	0.849	1.027
15	2.414	0.013	0.011	0.009	0.011	0.011	0.007	0.010	0.004
16	3.982	0.008	0.008	0.009	0.008	0.010	0.015	0.010	0.003
17	3.982	0.004	0.007	0.004	0.006	0.007	0.012	0.023	0.029
18	5.050	0.008	0.015	0.022	0.027	0.035	0.155	0.272	0.412
19	5.050	0.007	0.012	0.007	0.016	0.011	0.022	0.021	0.028
20	6.585	0.001	0.006	0.019	0.020	0.023	0.028	0.067	0.102
21	6.585	0.000	0.008	0.021	0.021	0.020	0.022	0.039	0.021
22	6.340	0.001	0.002	0.009	0.013	0.017	0.027	0.113	0.291
23	6.340	0.002	0.003	0.007	0.006	0.003	0.003	-0.007	-0.048
24	2.060	0.014	0.010	0.018	0.025	0.028	0.031	0.030	0.028
25	2.060	0.012	0.021	0.020	0.025	0.026	0.021	0.015	0.012
26	5.651	0.004	0.022	0.034	0.034	0.035	0.045	0.096	0.057
27	5.651	-0.003	0.004	0.006	0.007	0.004	0.005	0.007	0.006
28	5.148	0.013	0.028	0.030	0.027	0.028	0.071	0.027	0.048
29	5.148	0.005	0.014	0.011	0.013	0.012	0.026	0.008	0.017
30	3.208	0.026	0.026	0.033	0.045	0.149	0.307	0.286	0.423
31	3.208	0.046	0.047	0.050	0.058	0.128	0.092	0.054	0.060
32	1.318	0.000	0.007	0.014	0.026	0.025	0.022	0.017	0.029
33	1.318	0.012	0.012	0.017	0.018	0.015	0.013	0.007	0.007
34	5.800	0.002	0.009	0.019	0.025	0.035	0.050	0.138	0.156
35	5.800	0.001	0.028	0.048	0.047	0.051	0.063	0.119	0.087

Table 2 *continued*

Table 2 (continued)

ID	z	F70W	F90W	F115W	F150W	F200W	F277W	F356W	F444W
		(μJy)	(μJy)	(μJy)	(μJy)	(μJy)	(μJy)	(μJy)	(μJy)
(1)	(2)	(3)	(4)	(5)	(6)	(7)	(8)	(9)	(10)
36	7.877	-0.003	0.000	0.048	0.082	0.076	0.083	0.094	0.227
37	7.877	0.001	0.000	0.010	0.019	0.019	0.018	0.018	0.026
38	6.203	0.001	0.020	0.039	0.040	0.041	0.057	0.141	0.104
39	6.203	0.001	0.001	0.003	0.003	0.005	0.003	0.015	0.005
40	3.209	0.014	0.014	0.016	0.023	0.060	0.042	0.022	0.032
41	3.209	0.004	0.009	0.009	0.011	0.019	0.009	0.008	0.007
42	1.759	0.032	0.034	0.057	0.077	0.070	0.062	0.055	0.051
43	1.759	0.020	0.027	0.038	0.054	0.046	0.036	0.032	0.030
44	1.566	0.032	0.039	0.063	0.023	0.023	0.040	0.024	0.031
45	1.566	0.024	0.023	0.032	0.017	0.017	0.010	0.009	0.010
46	5.164	0.012	0.037	0.043	0.044	0.050	0.256	0.076	0.185
47	5.164	0.014	0.036	0.046	0.035	0.032	0.002	0.025	0.002
48	3.018	0.020	0.018	0.018	0.015	0.031	-0.013	-0.022	-0.036
49	3.018	0.024	0.024	0.027	0.038	0.068	0.205	0.221	0.365
50	7.040	-0.001	0.000	0.007	0.004	0.005	0.005	-0.001	-0.003
51	7.040	0.000	0.000	0.004	0.004	0.005	0.007	0.032	0.055
52	3.142	0.002	0.005	0.009	0.018	0.043	0.051	0.035	0.042
53	3.142	0.000	0.000	0.000	0.001	-0.002	-0.005	-0.005	-0.004
54	6.260	0.001	0.033	0.078	0.073	0.074	0.103	0.248	0.227
55	6.260	0.001	0.011	0.031	0.038	0.038	0.055	0.160	0.116
56	4.960	0.010	0.024	0.023	0.025	0.027	0.092	0.238	0.291
57	4.960	0.002	0.003	0.005	0.014	0.011	0.023	0.022	0.029
58	6.760	0.003	0.004	0.011	0.014	0.010	0.017	0.054	0.085
59	6.760	0.010	0.008	0.009	0.013	0.025	0.015	0.013	0.013
60	4.144	0.062	0.073	0.076	0.088	0.108	0.300	0.449	0.424
61	4.144	0.017	0.024	0.022	0.017	0.031	0.058	0.044	0.037

NOTE— (1) ID, (2) redshift (z_{spec} , where available, and otherwise z_{phot} , from Table 1), and JWST photometry from filters (3) F70W, (4) F90W, (5) F115W, (6) F150W, (7) F200W, (8) F277W, (9) F356W, and (10) F444W.

Table 3. Lensing-corrected Merger Analysis of Compact Pairs

IDs	Class	μ	z	θ	r	$\log M_{*,A}$	$\log M_{*,B}$	$\log M_{\text{tot}}$	v_{esc}	q	Type
				(arcsec)	(kpc)	(M_{\odot})	(M_{\odot})	(M_{\odot})	(km s^{-1})		
(1)	(2)	(3)	(4)	(5)	(6)	(7)	(8)	(9)	(10)	(11)	(12)
DD0, DD1	...	1.33	2.68556	0.12	0.83	8.35	7.73	9.94	299	0.240	Minor
DD2, DD3	BLAGN	1.68	4.01340	0.18	0.98	8.24	7.46	9.80	234	0.169	Minor
DD4, DD5	BLAGN	1.68	4.58294	0.13	0.66	8.36	7.22	9.88	315	0.072	Satellite
DD6, DD7	...	1.96	5.01506	0.13	0.61	7.83	6.91	9.37	182	0.120	Minor
DD8, DD9	...	1.46	7.23529	0.08	0.35	8.10	7.70	9.73	363	0.400	Major
DD10, DD11	...	2.84	2.34691	0.08	0.38	7.21	6.64	8.80	120	0.267	Major
DD12, DD13	...	2.60	3.65012	0.07	0.31	7.37	7.09	9.05	175	0.526	Major
DD14, DD15 [†]	LRD	1.40	2.41363	0.21	1.48	9.07	6.66	10.57	462	0.004	Satellite
DD16, DD17 [†]	LRD	1.74	3.98163	0.17	0.89	6.80	7.79	9.32	143	0.103	Minor
DD18, DD19 [†]	LRD	1.44	5.05000	0.18	0.99	9.19	8.02	10.71	667	0.068	Satellite
DD20, DD21 [†]	LRD	1.84	6.58456	0.15	0.62	8.64	7.96	10.22	477	0.206	Minor
DD22, DD23 [†]	LRD	1.59	6.34000	0.09	0.39	9.14	6.00	10.63	969	0.001	Satellite
DD24, DD25	...	1.44	2.05996	0.19	1.32	7.37	7.01	9.02	83	0.429	Major
DD26, DD27	...	1.44	5.65107	0.26	1.33	8.40	7.42	9.93	236	0.105	Minor
DD28, DD29 [†]	...	1.65	5.14826	0.25	1.25	8.21	7.76	9.83	216	0.354	Major
DD30, DD31 [†]	...	2.11	3.20763	0.18	0.96	8.72	7.87	10.27	407	0.142	Minor
DD32, DD33	...	1.39	1.31800	0.07	0.47	7.04	6.43	8.63	88	0.241	Minor
DD34, DD35 [†]	LRD	2.06	5.80000	0.15	0.62	8.70	8.45	10.38	578	0.558	Major
DD36, DD37 [†]	...	1.78	7.87713	0.24	0.91	9.12	8.18	10.66	656	0.115	Minor
DD38, DD39	...	1.77	6.20331	0.23	0.98	8.63	7.31	10.14	350	0.048	Satellite
DD40, DD41	...	1.36	3.20855	0.12	0.81	7.79	7.13	9.37	157	0.219	Minor
DD42, DD43	...	1.41	1.75942	0.23	1.65	7.52	7.29	9.21	92	0.588	Major
DD44, DD45	...	1.95	1.56558	0.10	0.62	7.07	6.58	8.68	82	0.323	Major
DD46, DD47 [†]	...	2.50	5.16353	0.15	0.60	8.61	6.65	10.11	430	0.011	Satellite
DD48, DD49 [†]	...	1.62	3.01792	0.08	0.50	6.00	8.73	10.22	536	0.002	Satellite
DD50, DD51 [†]	LRD	2.70	7.04000	0.11	0.36	6.00	8.25	9.75	366	0.006	Satellite
DD52, DD53	...	1.82	3.14236	0.08	0.47	7.77	6.00	9.26	183	0.017	Satellite
DD54, DD55 [†]	LRD	3.37	6.26000	0.09	0.28	8.70	8.41	10.37	840	0.511	Major
DD56, DD57 [†]	LRD	1.59	4.96000	0.06	0.29	8.98	7.98	10.51	978	0.100	Satellite
DD58, DD59 [†]	LRD	1.34	6.76000	0.17	0.82	8.72	7.90	10.27	445	0.153	Minor
DD60, DD61 [†]	LRD	1.90	4.14428	0.16	0.81	8.95	7.89	10.47	564	0.087	Satellite

NOTE— (1) “Double Dot” pairs IDs, (2) previously identified class (BLAGN or LRD), (3) delensed magnification, (4) redshift (z_{spec} , where available, and otherwise z_{phot} , from Table 1), (5) observed separation, (6) delensed physical separation ($r = r_{\text{obs}}/\sqrt{\mu}$), (7) and (8) delensed stellar masses of the two members ($M_* = M_*^{\text{obs}}/\mu$; labeled as “A” or “B” in the order of the listed IDs of the members), (9) total mass, assuming a dark matter ratio of 30, (10) escape velocity, (11) mass ratio, and (12) merger type based on the mass ratio: major ($q > 0.25$), minor ($0.10 < q \leq 0.25$), and satellite ($q \leq 0.10$). †At least one member of the pair satisfies the v-shape criterion for an LRD from [D. D. Kocevski et al. \(2025\)](#).

REFERENCES

- Ananna, T. T., Bogdán, Á., Kovács, O. E., Natarajan, P., & Hickox, R. C. 2024, *ApJL*, 969, L18
- Baggen, J. F. W., Scoggins, M. T., van Dokkum, P., et al. 2026, arXiv e-prints, arXiv:2602.02702
- Barger, A. J., Cowie, L. L., McKay, S. J., & Bauer, F. E. 2026, arXiv e-prints, arXiv:2605.24264
- Begelman, M. C., Volonteri, M., & Rees, M. J. 2006, *MNRAS*, 370, 289
- Bezanson, R., Labbe, I., Whitaker, K. E., et al. 2024, *ApJ*, 974, 92
- Chisholm, J., Berg, D. A., Boylan-Kolchin, M., et al. 2026, arXiv e-prints, arXiv:2602.15935
- de Graaff, A., Brammer, G., Weibel, A., et al. 2025, *Astronomy & Astrophysics*, 697, A189
- Furtak, L. J., Zitrin, A., Weaver, J. R., et al. 2023a, *MNRAS*, 523, 4568
- Furtak, L. J., Zitrin, A., Plat, A., et al. 2023b, *ApJ*, 952, 142
- Golubchik, M., Furtak, L. J., Allingham, J. F. V., et al. 2025, arXiv e-prints, arXiv:2512.02117
- Greene, J. E., Labbe, I., Goulding, A. D., et al. 2024, *ApJ*, 964, 39
- Harikane, Y., Zhang, Y., Nakajima, K., et al. 2023, *ApJ*, 959, 39
- Hausen, R., & Robertson, B. E. 2022, *Astronomy and Computing*, 39, 100586
- Heintz, K. E., Brammer, G. B., Watson, D., et al. 2025, *Astronomy & Astrophysics*, 693, A60
- Kocevski, D. D., Finkelstein, S. L., Barro, G., et al. 2025, *ApJ*, 986, 126
- Kroupa, P. 2001, *MNRAS*, 322, 231
- Labbe, I., Greene, J. E., Bezanson, R., et al. 2025, *ApJ*, 978, 92
- Larson, D., Dunkley, J., Hinshaw, G., et al. 2011, *ApJS*, 192, 16
- Lodato, G., & Natarajan, P. 2006, *MNRAS*, 371, 1813
- Lodato, G., & Natarajan, P. 2007, *MNRAS*, 377, L64
- Loeb, A., & Rasio, F. A. 1994, *ApJ*, 432, 52
- Maiolino, R., Scholtz, J., Curtis-Lake, E., et al. 2024, *A&A*, 691, A145
- Markwardt, C. B. 2009, in *Astronomical Society of the Pacific Conference Series*, Vol. 411, *Astronomical Data Analysis Software and Systems XVIII*, ed. D. A. Bohlender, D. Durand, & P. Dowler, 251
- Matthee, J., Naidu, R. P., Brammer, G., et al. 2024, *ApJ*, 963, 129
- Mazzolari, G., Gilli, R., Maiolino, R., et al. 2026, *A&A*, 706, A372
- Pacucci, F., Ferrara, A., & Kocevski, D. D. 2026, arXiv e-prints, arXiv:2601.14368
- Pacucci, F., & Narayan, R. 2024, *ApJ*, 976, 96
- Taylor, A. J., Finkelstein, S. L., Kocevski, D. D., et al. 2025, *ApJ*, 986, 165
- Treu, T., Roberts-Borsani, G., Bradac, M., et al. 2022, *ApJ*, 935, 110
- Volonteri, M., & Rees, M. J. 2005, *ApJ*, 633, 624
- Weaver, J. R., Cutler, S. E., Pan, R., et al. 2024, *ApJS*, 270, 7

ACKNOWLEDGEMENTS

We thank Anthony Taylor for helpful discussions. We gratefully acknowledge support for this research from the University of Wisconsin-Madison, Office of the Vice Chancellor for Research with funding from the Wisconsin Alumni Research Foundation (A. J. B.) and NASA grant 80NSSC22K0483 (L. L. C.).

Facilities: JWST